

A spider-like outflow in Barnard 5 - IRS 1: The transition from a collimated jet to a wide-angle outflow?

Luis A. Zapata¹*, Héctor G. Arce², Erin Brassfield³, Aina Palau⁴, Nimesh Patel³, and Jaime E. Pineda⁵

¹Centro de Radioastronomía y Astrofísica, UNAM campus Morelia, México

²Department of Astronomy, Yale University, P.O. Box 208101, New Haven, CT 06511, USA

³Harvard-Smithsonian Center for Astrophysics, 60 Garden Street, Cambridge MA 02138, USA

⁴Institut de Ciències de l'Espai (CSIC-IEEC), Campus UAB-Facultat de Ciències, Torre C5-parell 2, E-08193 Bellaterra, Catalunya, Spain

⁵Institute for Astronomy, ETH Zurich, Wolfgang-Pauli-Strasse 27, CH-8093 Zurich, Switzerland

Sent 2013

ABSTRACT

We present line and continuum observations made with the Submillimeter Array (SMA) of the young stellar object Barnard 5 - IRS1 located in the Perseus molecular cloud. Our $^{12}\text{CO}(2-1)$ line observations resolve the high-velocity bipolar northeast-southwest outflow associated with this source. We find that the outflowing gas shows different structures at three different velocity regimes, in both lobes, resulting in a spider-like morphology. In addition to the low-velocity, cone-like (wide-angle) lobes that have previously been observed, we report the presence of intermediate-velocity parabolic shells emerging very close to the Class I protostar, as well as high velocity molecular bullets that appear to be associated to the optical/IR jet emanating from this source. These compact high-velocity features reach radial velocities of about 50 km s^{-1} away from the cloud velocity. We interpret the peculiar spider-like morphology is a result of the molecular material being entrained by a wind with both a collimated jet-like component and a wide-angle component. We suggest the outflow is in a transitional evolutionary phase between a mostly jet-driven flow and an outflow in which the entrainment is dominated by the wide-angle wind component. We also detect $1300 \mu\text{m}$ continuum emission at the position of the protostar, which likely arises from the dusty envelope and disk surrounding the protostar. Finally, we report the detection of $^{13}\text{CO}(2-1)$ and $\text{SO}(6_5-5_4)$ emission arising from the outflow and the location of the young stellar object.

Key words: stars: formation — ISM: jets and outflows — ISM: individual objects (Barnard 5 - IRS1; HH 366 VLA 1)

1 INTRODUCTION

Bipolar outflows are an ubiquitous phenomena associated with star formation. The leading theories on the origin of protostellar outflows indicate that they are generated through the interaction of ionized disk material and the magnetic fields from the forming star and/or disk (Li et al. 2014, and references therein). Protostellar winds entrain the host cloud's molecular gas thereby producing molecular outflows (e.g. Arce et al. 2007).

There is substantial observational evidence showing that molecular outflows from low-mass young stars tend to have relatively well-collimated lobes early in their development and then evolve to have wider opening angle flows at later stages (Richer et al. 2000; Arce & Sargent 2006; Seale & Looney 2008). However, there is no consensus on the detailed physics that produce

this evolutionary trend in molecular outflows. It has been proposed that jet axis wandering (precession) could produce wider cavities as the protostar evolves (Masson & Chernin 1993). However, in most sources the opening angle of the precession cone is smaller than the observed wide-angle outflow cavity (e.g., Reipurth et al. 2000). A second possibility is that protostellar winds have both a collimated and a wide-angle component, and the observed molecular outflow is predominantly driven by one of the two components, depending on the age of the protostar (e.g., Shang et al. 2006; Romanova et al. 2009). In this scenario the opening angle and axis direction of the wind arising from the protostar/disk system remain approximately constant, but the wind increasingly disperses more of the circumstellar gas, thereby creating wider outflow cavities, as the protostar evolves and the circumstellar envelope decreases in density (e.g., Offner et al. 2011).

Barnard 5 - IRS 1 (hereafter, B5-IRS1) is a young stellar object located at the eastern end of the Perseus molecular cloud

* E-mail: lzapata@crya.unam.mx

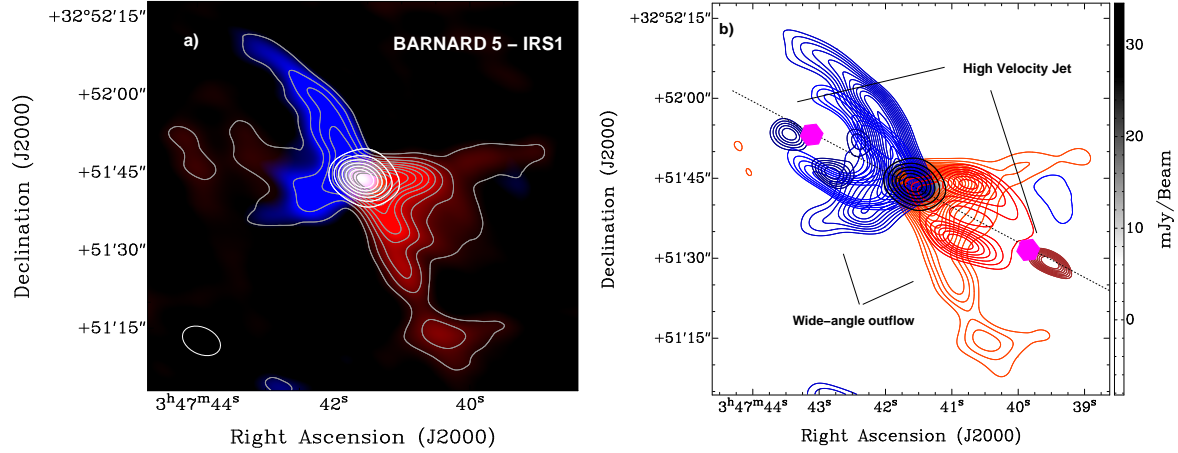


Figure 1. **a)** SMA integrated intensity (moment 0) color scale and contour map of the $^{12}\text{CO}(2-1)$ emission (grey contours), and the continuum emission at $1300\ \mu\text{m}$ (white contours) from B5-IRS 1. The blue color scale represents blueshifted gas, while the red color scale represents redshifted gas. The integrated velocity range for the blueshifted side is from -50.9 to $+6.2\ \text{km s}^{-1}$, while for the redshifted side is from $+14.7$ to $+70.8\ \text{km s}^{-1}$. The white contours range from 35% to 85% of the peak emission, in steps of 10%. The peak of the continuum emission is $0.032\ \text{Jy beam}^{-1}$. The grey contours range from 10% to 87% of the peak emission, in steps of 7%. The peak of the $^{12}\text{CO}(2-1)$ line emission is $150\ \text{Jy beam}^{-1}\ \text{km s}^{-1}$. The emission peak here is the arithmetic sum of the total integrated CO emission. The synthesized beam of the continuum image is shown in the lower left corner. **b)** Integrated intensity map of the Barnard 5 IRS1 $^{12}\text{CO}(2-1)$ outflow at different velocity ranges. The different blue and red color tones of the contours represent different range of velocities with the lighter (darker) hues representing lower (higher) outflow velocities. The low-velocity blue and red ranges are $[-4.3$ to $+6.2\ \text{km s}^{-1}]$ and $[+14.7$ to $+24.2\ \text{km s}^{-1}]$. The intermediate-velocity ranges are $[-39.0$ to $-15.9\ \text{km s}^{-1}]$ and $[+35.1$ to $+59.7\ \text{km s}^{-1}]$, while the high-velocity ranges are $[-50.9$ to $-40.3\ \text{km s}^{-1}]$ and $[+60.2$ to $+70.8\ \text{km s}^{-1}]$. The high velocity bullets show a larger spread of velocities (see Figure 4), however, for clarity, we choose these slightly narrower high-velocity windows. The contours for the different blue and red contours range from about 30% to 90% of the peak emission, in steps of 5%. In the high-velocity emission the contours start from 50% the peak of the line emission. The two pink hexagons mark the positions of the strongest H_2 and $\text{H}\alpha$ knots reported by Yu et al. (1999).

complex at a distance of about 240 pc (Hirota et al. 2011). This object is embedded in a dense core with a filamentary structure (Pineda et al. 2011). B5-IRS1 has a bolometric luminosity of $\sim 5\ L_{\odot}$ (Beichman et al. 1984; Evans et al. 2009) and drives a giant bipolar flow associated with two clusters of HH objects: HH 366 E to the northeast and HH 366 W to the southwest (Bally et al. 1996; Yu et al. 1999). A molecular outflow with a bipolar wide-angle morphology and a southwest-northeast orientation is found at the base of these HH objects (Fuller et al. 1991; Langer et al. 1996; Velusamy & Langer 1998). Both the blueshifted lobe (northeast of the source) and the redshifted lobe (southwest of the source) show a wide-angle cone-like structure with a projected opening angle of about 90° (Langer et al. 1996). Near infrared and optical images shown by Yu et al. (1999) reveal H_2 and $\text{H}\alpha$ emission within $20''$ of B5-IRS1, arising from a jet that bisects the limb-brightened CO cones. Yu et al. (1999) suggested that the presence of both axial jet-knots and a wide-angle cavity implies that the central source may simultaneously power both a jet and a wide-angle wind.

In this paper, we present new line and continuum Submillimeter Array¹ (SMA) observations of the young star B5-IRS1. These observations reveal further structure in the bipolar outflow associated with this young stellar object and show that it has a peculiar morphology.

2 OBSERVATIONS

The observations were made with the SMA, and were collected on 2007 September 13, when the array was in its subcompact configuration. The 21 independent baselines in this configuration ranged in projected length from 5 to 35 $k\lambda$. The phase reference center for the observations was set to $\alpha_{J2000.0} = 03^{\text{h}}47^{\text{m}}41^{\text{s}}.60$, $\delta_{J2000.0} = +32^\circ51'43''.5$. Two frequency bands, centered at 230.53799 GHz (Upper Sideband) and 220.53799 GHz (Lower Sideband) were observed simultaneously. The primary beam of the SMA at 230 GHz has a FWHM of about $50''$, and the continuum emission arising from B5-IRS1 falls well within it. The line emission, on the other hand, extends beyond the FWHM of the primary beam, so we corrected the images for the primary beam attenuation.

The SMA digital correlator was configured to have 24 spectral windows (“chunks”) of 104 MHz and 128 channels each. This provided a spectral resolution of 0.812 MHz ($\sim 1\ \text{km s}^{-1}$) per channel. Observations of Uranus provided the absolute scale for the flux density calibration. The gain calibrators were the quasars 3C 111 and 3C 84, while 3C 454.3 was used for bandpass calibration. The uncertainty in the flux scale is estimated to be between 15 and 20%, based on the SMA monitoring of quasars.

The data were calibrated using the IDL superset MIR, originally developed for the Owens Valley Radio Observatory (OVRO, Scoville et al. 1993) and adapted for the SMA.² The calibrated data were imaged and analyzed in the standard manner using

¹ The Submillimeter Array (SMA) is a joint project between the Smithsonian Astrophysical Observatory and the Academia Sinica Institute of Astronomy and Astrophysics, and is funded by the Smithsonian Institution and the Academia Sinica.

² The MIR-IDL cookbook by C. Qi can be found at <http://cfa-www.harvard.edu/~cqi/mircook.html>.

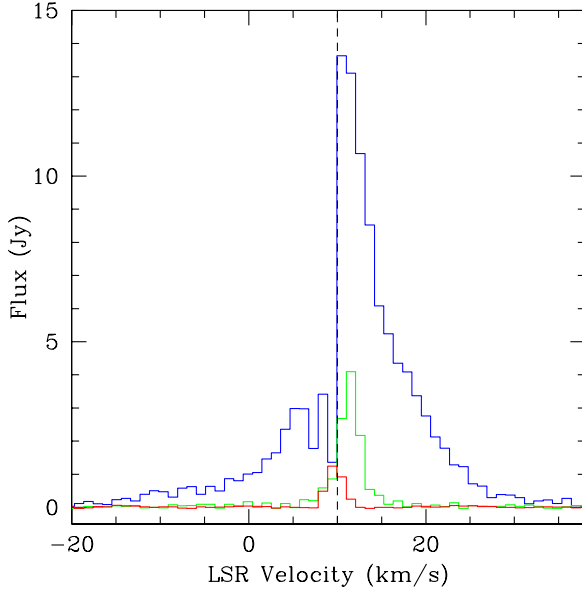


Figure 2. Sum spectra of the three lines detected towards B5-IRS1: $^{12}\text{CO}(2-1)$ (blue), $^{13}\text{CO}(2-1)$ (green), and $\text{SO}(6_5-5_4)$ (red). The sum spectra were obtained from an area delimited by a $45'' \times 45''$ square for $^{12}\text{CO}(2-1)$, and a $20'' \times 20''$ square for $^{13}\text{CO}(2-1)$ and $\text{SO}(6_5-5_4)$, all centered at the position of the source. The vertical dashed line represents the location of the systemic velocity of the cloud, $V_{\text{LSR}} \sim 10.0 \text{ km s}^{-1}$. The spectra were obtained with the task VELPLOT of MIRIAD.

the MIRIAD (Sault et al. 1995) and KARMA (Gooch 1996) softwares³. A 1300 μm continuum image was obtained by averaging line-free channels in the lower sideband with a bandwidth of about 2 GHz. For the line emission, the continuum was also removed. For the continuum emission, we set the ROBUST parameter of the task INVERT to 0 to obtain an optimal compromise between resolution and sensitivity, while for the line emission we set this to -2 in order to obtain a higher angular resolution. The resulting r.m.s. noise for the continuum image was about 2 mJy beam^{-1} at an angular resolution of $7''.74 \times 4''.87$ with a P.A. = 66.3° . The r.m.s. noise in each channel of the spectral line data was about 80 mJy beam^{-1} at an angular resolution of $7''.51 \times 4''.18$ with a P.A. = 63.2° .

3 RESULTS AND DISCUSSION

3.1 Continuum

In Figure 1, we show the 1300 μm continuum image resulting from these millimeter SMA observations. We only detect a single source that is associated with B5-IRS 1 at the position of $\alpha_{J2000.0} = 03^{\text{h}}47^{\text{m}}41^{\text{s}}.5$, $\delta_{J2000.0} = +32^\circ51'43''.8$, with a positional error of less than $1''.0$. From a Gaussian fit to the continuum emission we obtain that the flux density and peak intensity values of this compact source at this wavelength are $54 \pm 8 \text{ mJy}$ and $31 \pm 5 \text{ mJy beam}^{-1}$, respectively. The Gaussian fit was also used to determine that the deconvolved size for this continuum source is $5''.5 \pm 0''.5 \times 4''.0 \pm 0''.6$ with a P.A. = $-28^\circ \pm 10^\circ$. Therefore, at the distance of the

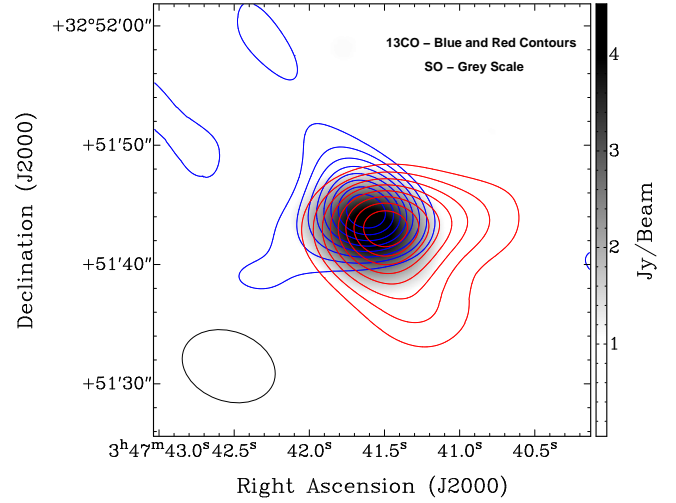


Figure 3. Moment zero map of the SO line emission (grey scale) shown in combination with the blue- and red-shifted ^{13}CO emission (blue and red contours, respectively). For $\text{SO}(6_5-5_4)$ the velocity integration range is from +7 to +12 km s^{-1} . For $^{13}\text{CO}(2-1)$ the velocity integration range for the blueshifted lobe is from +6.5 to +8.6 km s^{-1} , while for the redshifted lobe is from +11.8 to +16.0 km s^{-1} . The blue and red contours range from 20% to 90% of their respective peak emission, in steps of 10%. The peak of the blue and red emission are 6.4 and $2.5 \text{ Jy beam}^{-1} \text{ km s}^{-1}$, respectively. The synthesized beam of the SO and the ^{13}CO lines is shown in the lower left corner. The grey-scale bar on the right pertain to the SO line emission map.

Perseus molecular cloud complex the size of the continuum source is about 1200 AU.

Following Hildebrand (1983) and assuming optically thin isothermal dust emission, a gas-to-dust ratio of 100, a dust temperature of 30 K, a dust mass opacity $\kappa_{1300\mu\text{m}} = 1.1 \text{ cm}^2 \text{ g}^{-1}$ (Ossenkopf & Henning 1994), and that this object is located at 240 pc, we estimate the total mass associated with the dust continuum emission to be $0.02 M_\odot$, this in a good agreement with the value obtained by Brassfield & Bourke (2011). However, we remark that the mass estimate presented in Brassfield & Bourke (2011) was obtained using a restricted UV-range trying to avoid the envelope contribution.

The millimeter continuum emission is probably tracing the envelope and the circumstellar disk surrounding B5-IRS 1. Furthermore, we remark that the detected continuum emission could be partially optically thick, and therefore the reported mass estimate is a lower limit.

3.2 Spectral Lines

In Figure 2, we show the lines that were detected in the two sidebands and that are discussed throughout this article. We simultaneously detected three lines, the $^{12}\text{CO}(2-1)$ at a rest frequency of about 230.5 GHz, $^{13}\text{CO}(2-1)$ at a rest frequency of about 220.5 GHz, and the $\text{SO}(6_5-5_4)$ line at a rest frequency of about 219.9 GHz. The exact values for the rest frequency of these lines can be found in the database for astronomical spectroscopy: <http://splatalogue.net>. The sum spectra of $^{13}\text{CO}(2-1)$ and $\text{SO}(6_5-5_4)$ are narrower and fainter compared to the $^{12}\text{CO}(2-1)$ spectrum.

³ The calibrated data can be obtained from: http://www.cfa.harvard.edu/rtdc/sciImages/070913_125512_b5irs1.html

The former have a FWHM between 3-5 km s⁻¹, while the latter has a FWHM of 20 km s⁻¹. The sum spectra of ¹²CO and ¹³CO show wings at high velocities that are attributed to the presence of molecular outflows. This is confirmed by our integrated intensity maps showing a clear bipolar structure, see Figures 1 and 3.

In Figure 1a we show the velocity-integrated intensity, or zero-moment map, of ¹²CO(2-1) for both the blue and red outflow lobes. The velocity range of integration for the blueshifted lobe is from -50.9 to +6.2 km s⁻¹, while for the redshifted lobe is from +14.7 to +70.8 km s⁻¹. With our SMA observations we detect a substantially larger spread of velocities because the SMA data have significantly better sensitivity than previous studies (see Velusamy & Langer 1998). The left panel in Figure 1 shows the wide-angle bipolar outflow that has been reported in previous high-angular resolution studies of this source (Langer et al. 1996; Velusamy & Langer 1998). In addition, our higher sensitivity and fidelity maps reveal new features in the outflow, especially at high velocities, that are shown in Figure 1b.

In Figure 1b, we split the range of integration into three different velocity ranges in both the blueshifted and redshifted lobes. The velocity ranges were selected such that each velocity range reveals distinct features that appear to be similar (symmetrical) in both lobes of the molecular outflow. These features are clearly separated in velocity (and space) and do not appear to be a single continuous structure in the outflow. At low velocities the wide-angle bipolar outflow reported by previous studies is clearly seen. Our map reveals that the low-velocity blueshifted lobe has a parabolical morphology, while the redshifted lobe is a conical (or triangular) shape. The vertices of the cones have a projected opening angle of about 90° for the blue lobe and about 80° for the red lobe. At intermediate velocities the outflow shows parabolical lobes that have narrower opening angles than the low-velocity outflow gas; we measured an opening angle of 50° for the red and 60° for the blue lobe. At high velocities we detect very compact structures (or bullets) in the blue and red lobes that are equidistant from the position of the source. Including the maps of all three different velocity ranges, for both lobes, together in the same figure the outflow shows a “spider-like” structure (see Figure 1b).

In Figure 1b, we also included the positions of the strongest knots from the jet mapped in H₂ and H α by Yu et al. (1999). There is a good correspondence between the molecular and optical knots with a small offset of about 5'' (or ~ 1200 AU) between corresponding peaks, with both molecular bullets being farther away from the source than the optical/IR knots. One possible explanation to this offset is that the knots and the molecular bullets are produced by the same mass ejection episode, and that the difference in position is caused by the fact that the two different datasets were taken approximately a decade apart. A tangential velocity of approximately 570 km s⁻¹ would cause the observed positional offset between the optical knot and the molecular bullet. Such very high velocities have been observed in several Herbig-Haro objects (e.g. HH 111; HH 39 Jones & Herbig 1982; Schwartz et al. 1984; Hartigan et al. 2001). We note that both the blueshifted and redshifted bullets are almost symmetrical in position (with respect to the source) which suggests that they were both ejected in the same mass ejection event. We tentatively suggest that the optical and molecular bullets are different manifestations of the same mass ejection episode. However, more optical/IR and millimeter data are needed to confirm this.

Assuming local thermodynamic equilibrium (LTE), and that the ¹²CO(2-1) molecular emission is optically thin, we estimate the

outflow mass using the following equation:

$$\frac{M(H_2)}{M_\odot} = 6.3 \times 10^{-20} m(H_2) X_{\frac{H_2}{CO}} \left(\frac{c^2 d^2}{2k\nu^2} \right) \frac{\exp\left(\frac{5.5}{T_{ex}}\right) \int S_\nu dv \Delta\Omega}{\left(1 - \exp\left[-\frac{11.6}{T_{ex}}\right]\right)},$$

where all units are in cgs, $m(H_2)$ is mass of the molecular hydrogen with a value of 3.34×10^{-24} g, $X_{\frac{H_2}{CO}}$ is the fractional abundance between the carbon monoxide and the molecular hydrogen (10^4), c is the speed of light with a value of 3×10^{10} cm s⁻¹, k is the Boltzmann constant with a value of 1.38×10^{-16} erg K⁻¹, ν is the rest frequency of the CO line in Hz, d is distance (240 pc), a parsec is equivalent to 3.08×10^{18} cm, S_ν is the flux density of the CO (Jansky), a Jansky is equivalent to 1.0×10^{-23} erg s⁻¹ cm⁻² Hz⁻¹, dv is the velocity range in cm s⁻¹, $\Delta\Omega$ is the solid angle of the source in steradians, and T_{ex} is excitation temperature taken to be 50 K. Using only emission above 4- σ in every velocity channel map, we estimate a mass for the outflow powered by B5-IRS 1 to be $7 \times 10^{-3} M_\odot$. This value is consistent with the mass of other molecular outflows powered by young low-mass protostars, see Wu et al. (2004). The mass estimated here is only a lower limit because the CO emission is likely to be optically thick (see, e.g., Dunham et al. 2014).

We also estimate a kinematical energy ($E_k = \sum_i \frac{1}{2} \cdot m \cdot v_i^2$) of 2×10^{44} ergs, and an outflow momentum ($p = \sum_i m \cdot v_i$) of $0.5 M_\odot$ km s⁻¹. From Figure 1, we estimate a dynamical age approximately of 700 years, which results in a mechanical luminosity ($L = \frac{E_k}{t}$, where E_k is the kinematical energy and t is the dynamical age) of about $2 L_\odot$. The dynamical age is estimated assuming a size for the molecular outflow of 30'' and a velocity of 50 km s⁻¹. These estimates do not take into consideration the inclination of the outflow with respect to the line-of-sight (which is thought to be high for this source, see Yu et al. 1999).

In Figure 3, we show the integrated intensity map of the SO(6₅-5₄) and the ¹³CO(2-1) emission. The SO line emission reveals a single compact object associated with the continuum source in the position of B5-IRS 1, and does not show any clear velocity gradient in our data. On the other hand, the ¹³CO(2-1) emission reveals cone-like lobes in the inner region of the bipolar outflow.

3.3 Shells from a spider-like outflow

In Figure 4 we present the Positional-Velocity Diagram (PVD) of the ¹²CO(2-1) emission along the outflow axis (P.A. = 67.1°). The PVD shows two structures at different velocity ranges. The main structure in the middle of the diagram, at low to intermediate velocities (within outflow velocities of 30 km s⁻¹), shows a rotated “X” morphology. Comparing the molecular outflow properties predicted by different models presented in Arce et al. (2007) with the velocity structure (from the PVD) and the cone-like morphology in both lobes of the B5-IRS 1 outflow (in Figure 1a) we propose that this outflow is mostly driven by a wide-angle wind, as concluded by Langer et al. (1996).

There is also evidence, from the optical and infrared observations by Yu et al. (1999) and our SMA data (*i.e.*, the high-velocity bullets shown in Figure 1b), that B5-IRS 1 powers a very collimated (jet-like) wind. The molecular outflow jet component is also observed in our PVD as a structure at high outflow velocities distinct from the central rotated “X” structure in Figure 4. This is most evident in the redshifted lobe where faint emission, at offsets more negative than -10'' and at LSR velocities greater than +20 km s⁻¹ (and up to about +60 km s⁻¹), shows outflow velocity increasing with offset from the source, as expected in a jet-driven molecular outflow (see, *e.g.*, Lee et al. 2000, 2001). The PVD in Figure 4

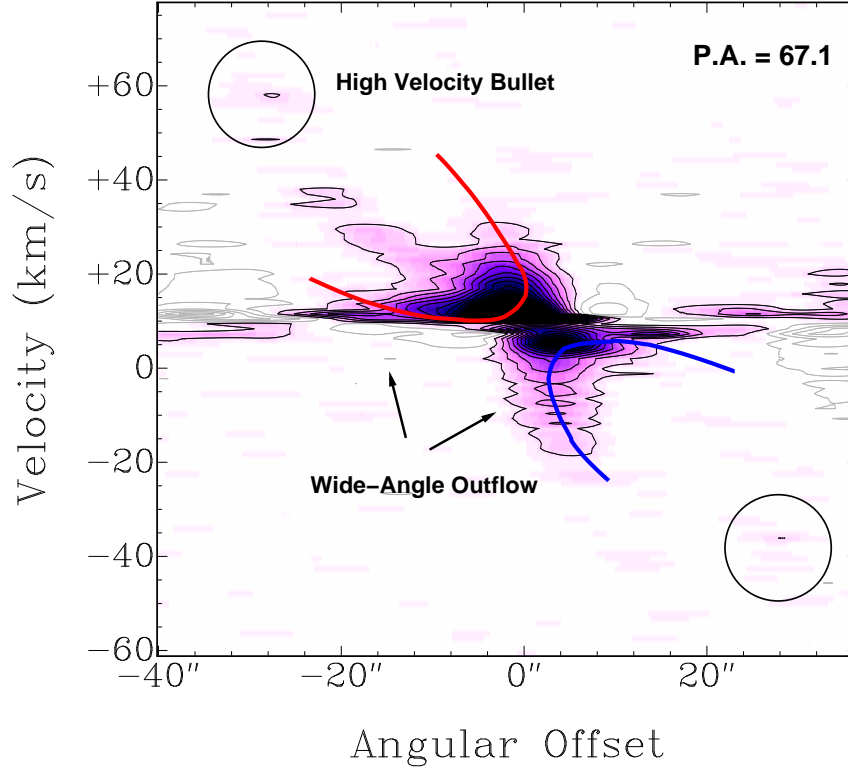


Figure 4. Position velocity diagram (PVD) along the axis of the outflow that is shown in Figure 1. The PVD was made at a position angle of 67.1° . The black contours range from 6% to 90% of the peak emission, in steps of 4%. The peak of the line emission is 6 Jy beam^{-1} . The grey contours represent the negative emission arising mainly from velocities close to the cloud's systemic velocity and have the same value as the black contours, but negative. The curves mark the different structures found in our PVD. The circles mark the highest velocity features in the outflow. Velocity is shown with respect to the Local Standard of Rest (LSR).

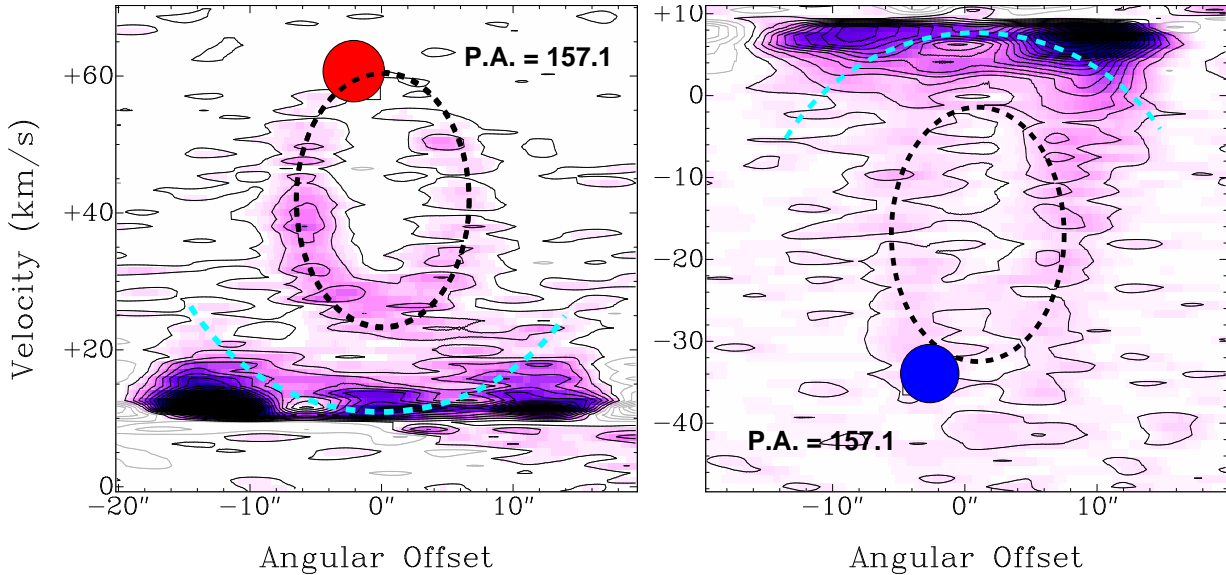


Figure 5. Left panel: PVD perpendicular to the outflow axis in the redshifted lobe. The PVD was made at a position angle of 157.1° . The contour levels and the peak emission are the same as Figure 4. Right panel: The same as in the left panel, but for the blueshifted lobe. The contour levels and the peak emission are the same as Figure 4. The blue and red dots represent the position and velocities of the high-velocity bullets shown in Figure 1b. The dashed curves mark the different structures found in the PVDs. Both PVDs were made approximately $15''$ away from the continuum source in both sides of the outflow.

shows that the molecular bullets in both lobes reach outflow velocities of about 50 km s^{-1} .

In Figure 5 we present position-velocity diagrams of both outflow lobes, along cuts perpendicular to the outflow axis (P.A. = 157.1°). These PVDs present different structures compared to those shown in Figure 4. At low outflow velocities ($\lesssim 10 \text{ km s}^{-1}$) there are two bright curved structures that have similar velocity ranges in both outflow lobes, and are related to the low-velocity and very wide-angle structures seen in Figure 1b. In addition, there are two (faint) ring-like structures in both sides of the flow at intermediate velocities (at outflow velocities of about 10 to 45 km s^{-1}). Such structures, in position-velocity space, are reminiscent of radially expanding shells or bubbles (see for example Zapata et al. 2011; Arce et al. 2011), but are also similar to the elliptical structures expected in the PVD of a jet with a low inclination with respect to the plane of the sky (see Figure 26 of Lee et al. 2000). As discussed above, the integrated intensity map at intermediate velocities show narrow parabolic structures, very different from the circular (or semi-circular) structures associated with radially expanding bubbles. Furthermore, the observed structure is somewhat similar to the structures seen in young (Class 0) jet-powered molecular outflows like L1448 (Bachiller et al. 1995), L1157 (Gueth et al. 1996) and HH 211 (Gueth & Guilloteau 1999; Palau et al. 2006; Lee et al. 2007). In these young sources the molecular outflow cavities have a moderate opening angle (similar to the intermediate-velocity structures we detect in B5-IRS1) that are presumably formed by the passage of jet bow-shocks, consistent with the bow shock-driven molecular outflow model of Raga & Cabrit (1993). It therefore seems more likely that the observed intermediate-velocity features are caused by propagating bow shocks in a jet, or highly collimated wind. The high-velocity bullets are located at the tips of the intermediate-velocity elliptical structure in the position-velocity diagrams shown in Figure 5 (and at the far ends of the PVD shown in Figure 4). Hence, it seems possible that these high-velocity features are tracing the tip (or head) of the bow-shock responsible for the intermediate-velocity cavities.

3.4 Nature of the morphology of the B5-IRS1 outflow

One of the most striking characteristics of the B5-IRS1 outflow is the different structures observed at different ranges of velocities. As discussed above, the high-velocity bullets and intermediate velocity structure are driven by a collimated (jet-like) wind, while the low-velocity lobes are consistent with being formed by a wide-angle wind. An increasing number of outflows have been observed that show two components (a wide-angle structure and a collimated feature). They include L1551 (Itoh et al. 2000), HH 46/47 (Velusamy et al. 2007; Arce et al. 2013), Cepheus HW2 (Torrelles et al. 2011), and Source I (Matthews et al. 2010; Zapata et al. 2012). However, to our knowledge, none of these outflows show a spider-like structure like the one we observe in B5-IRS 1.

These “dual component” molecular outflows are generally explained by assuming that the underlying protostellar wind that entrains the surrounding ambient gas has a wide-angle morphology with a narrow component (with a much higher outflow momentum rate) along the wind axis as in the X-wind models of Shang et al. (2006) and disc-magnetosphere boundary outflow launching models of Romanova et al. (2009). The spider-like morphology of the B5-IRS 1 molecular outflow may be explained with these kinds of models. One hypothesis for the observed evolutionary trend in outflow opening angle is that the observed molecular outflow (pro-

duced by the interaction between the protostellar wind and the surrounding ambient gas) is mostly driven by one of the two different components, depending on the evolutionary stage of the protostar and the density distribution of the circumstellar material. During the early deeply embedded stage of protostellar evolution (Class 0) only the high-momentum component along the outflow axis is able to puncture through the dense circumstellar envelope, producing a collimated (jet-like) outflow. At later stages (*i.e.*, Class I and II), after the envelope loses mass through outflow entrainment and infall onto the protostar, the wider component will be able to entrain the remaining circumstellar material at larger angles away from the outflow axis. If such picture is correct, we should then expect a transitional phase when there is little or no molecular gas along the outflow axis, yet enough molecular gas at intermediate angles (*i.e.*, between the outflow axis and the edge of the wide-angle wind) that would result in a molecular outflow with a component that is approximately midway between the collimated and wide-angle components, and a faint (or no) on-axis component.

We suggest this scenario explains the spider-like structure seen in B5-IRS1, which in fact may be considered a young Class I source (based on its spectral energy distribution, *e.g.*, Arce & Sargent 2006) and hence likely to be in an evolutionary phase close to the transition between Class 0 and Class I (see also Yu et al. 1999). We argue that in B5-IRS1 the molecular outflow material is detected along (and within 30° of) the outflow axis (as shown by the high-velocity bullet and the intermediate-velocity structure) because there is still enough molecular material in the cavity for it to be entrained by the collimated (jet) component of the wind (as expected in a young source). However, as seen in Figure 1 (where the integrated intensity of the outflowing CO emission is dominated by the very wide angle structure) most of the entrainment is taking place at larger angles from the axis where the wide-angle wind is currently interacting with the denser parts of the surrounding envelope.

SUMMARY

We observed in the millimeter regime the dust and molecular gas surrounding the young stellar object B5-IRS 1 using the Submillimeter Array. Our conclusions are as follow:

- The millimeter dust continuum emission reported here is tracing the envelope and circumstellar disk surrounding B5-IRS 1.
- Our $^{12}\text{CO}(2-1)$ observations resolve the bipolar northeast-southwest outflow associated with B5-IRS 1 and find that its morphology is reminiscent of a “spider”, where three velocity components with different morphologies are present in each lobe.
- In addition to detecting the previously observed wide-angle cone-like lobes, our observations for the first time reveal the presence of intermediate-velocity, parabolic shells emerging very close to the young stellar object as well as high-velocity compact molecular bullets which we argue are associated with the optical/IR jet in this source. These high-velocity features reach outflow (radial) velocities of about 50 km s^{-1} .
- We interpret the peculiar spider-like morphology as a result of the molecular material being entrained by a wind in which the momentum has an angular dependence (*i.e.*, larger towards the outflow axis). We believe the peculiar outflow morphology is evident in this source because it is in a transitional evolutionary phase, at a stage that is slightly older than the phase in which the outflow is completely dominated by the on-axis (collimated) part of the wind, but

slightly younger than the stage in which the outflow entrainment is fully dominated by the wide-angle component of the wind.

- We report the detection $^{13}\text{CO}(2-1)$ and $\text{SO}(6_5-5_4)$ emission, which arises from the outflow and the vicinity of B5-IRS1.

We conclude that the protostar B5-IRS 1 is a great laboratory to study the process of outflow formation and evolution. Further observations at different wavelengths and at higher angular and velocity resolution are needed to better understand its kinematics as well its launching and entrainment mechanisms.

ACKNOWLEDGMENTS

L.A.Z. acknowledge the financial support from DGAPA, UNAM, and CONACyT, México. H.G.A. acknowledges support from his NSF CAREER award AST-0845619. A.P. is supported by the Spanish MICINN grant AYA2011-30228-C03-02 (co-funded with FEDER funds), and by the AGAUR grant 2009SGR1172 (Catalonia).

REFERENCES

- Arce, H. G., Borkin, M. A., Goodman, A. A., Pineda, J. E., & Beaumont, C. N. 2011, *ApJ*, 742, 105
- Arce, H. G., Mardones, D., Corder, S. A., et al. 2013, *ApJ*, 774, 39
- Arce, H. G., & Sargent, A. I. 2006, *ApJ*, 646, 1070
- Arce, H. G., Shepherd, D., Gueth, F., et al. 2007, *Protostars and Planets V*, 245
- Bachiller, R., Guilloteau, S., Dutrey, A., et al. 1995, *A&A*, 299, 857
- Bally, J., Devine, D., & Alten, V. 1996, *ApJ*, 473, 921
- Beichman, C. A., Jennings, R. E., Emerson, J. P., et al. 1984, *ApJL*, 278, L45
- Brassfield, E., & Bourke, T. L. 2011, *Bulletin of the American Astronomical Society*, 43, #340.09
- Dunham, M. M., Arce, H. G., Mardones, D., et al. 2014, *ApJ*, 783, 29
- Evans, N. J., II, Dunham, M. M., Jørgensen, J. K., et al. 2009, *ApJS*, 181, 321
- Fuller, G. A., Myers, P. C., Welch, W. J., et al. 1991, *ApJ*, 376, 135
- Gooch, R. 1996, *Astronomical Data Analysis Software and Systems V*, 101, 80
- Gueth, F., & Guilloteau, S. 1999, *A&A*, 343, 571
- Gueth, F., Guilloteau, S., & Bachiller, R. 1996, *A&A*, 307, 891
- Hartigan, P., Morse, J. A., Reipurth, B., Heathcote, S., & Bally, J. 2001, *ApJL*, 559, L157
- Hirota, T., Honma, M., Imai, H., et al. 2011, *PASJ*, 63, 1
- Hildebrand, R. H. 1983, *Quarterly Journal of the Royal Astronomical Society*, 24, 267
- Itoh, Y., Kaifu, N., Hayashi, M., et al. 2000, *PASJ*, 52, 81
- Jones, B. F., & Herbig, G. H. 1982, *AJ*, 87, 1223
- Krist, J. E., Stapelfeldt, K. R., Hester, J. J., et al. 2008, *AJ*, 136, 1980
- Langer, W. D., Velusamy, T., & Xie, T. 1996, *ApJL*, 468, L41
- Lee, C.-F., Ho, P. T. P., Palau, A., et al. 2007, *ApJ*, 670, 1188
- Lee, C.-F., Mundy, L. G., Reipurth, B., Ostriker, E. C., & Stone, J. M. 2000, *ApJ*, 542, 925
- Lee, C.-F., Stone, J. M., Ostriker, E. C., & Mundy, L. G. 2001, *ApJ*, 557, 429
- Li, Z.-Y., Banerjee, R., Pudritz, R. E., et al. 2014, arXiv:1401.2219
- Liseau, R., & Sandell, G. 1986, *ApJ*, 304, 459
- Machida, M. N., & Hosokawa, T. 2013, *MNRAS*, 431, 1719
- Masson, C. R., & Chernin, L. M. 1993, *ApJ*, 414, 230
- Matthews, L. D., Greenhill, L. J., Goddi, C., et al. 2010, *ApJ*, 708, 80
- Offner, S. S. R., Lee, E. J., Goodman, A. A., & Arce, H. 2011, *ApJ*, 743, 91
- Ossenkopf, V., & Henning, T. 1994, *A&A*, 291, 943
- Pech, G., Zapata, L. A., Loinard, L., & Rodríguez, L. F. 2012, *ApJ*, 751, 78
- Palau, A., Ho, P. T. P., Zhang, Q., et al. 2006, *ApJL*, 636, L137
- Pineda, J. E., Goodman, A. A., Arce, H. G., et al. 2011, *ApJL*, 739, L2
- Richer, J. S., Shepherd, D. S., Cabrit, S., Bachiller, R., & Churchwell, E. 2000, *Protostars and Planets IV*, 867
- Raga, A., & Cabrit, S. 1993, *A&A*, 278, 267
- Reipurth, B., Yu, K. C., Heathcote, S., Bally, J., & Rodríguez, L. F. 2000, *AJ*, 120, 1449
- Romanova, M. M., Ustyugova, G. V., Koldoba, A. V., & Lovelace, R. V. E. 2009, *MNRAS*, 399, 1802
- Torrelles, J. M., Patel, N. A., Curiel, S., et al. 2011, *MNRAS*, 410, 627
- Sault, R. J., Teuben, P. J., & Wright, M. C. H. 1995, *Astronomical Data Analysis Software and Systems IV*, 77, 433
- Scoville, N. Z., Carlstrom, J. E., Chandler, C. J., et al. 1993, *PASP*, 105, 1482
- Seale, J. P., & Looney, L. W. 2008, *ApJ*, 675, 427
- Shang, H., Allen, A., Li, Z.-Y., et al. 2006, *ApJ*, 649, 845
- Schwartz, R., Jones, B. F., & Sirk, M. 1984, *AJ*, 89, 1735
- Velusamy, T., & Langer, W. D. 1998, *Nature*, 392, 685
- Velusamy, T., Langer, W. D., & Marsh, K. A. 2007, *ApJL*, 668, L159
- Yu, K. C., Billawala, Y., & Bally, J. 1999, *AJ*, 118, 2940
- Wu, Y., Wei, Y., Zhao, M., et al. 2004, *A&A*, 426, 503
- Zapata, L. A., Loinard, L., Schmid-Burgk, J., et al. 2011, *ApJL*, 726, L12
- Zapata, L. A., Rodríguez, L. F., Schmid-Burgk, J., et al. 2012, *ApJL*, 754, L17